

UV Raman lidar measurements of relative humidity for the characterization of cirrus cloud microphysical properties

P. Di Girolamo¹, D. Summa¹, R.-F. Lin^{2,3}, T. Maestri⁴, R. Rizzi⁴, and G. Masiello¹

¹Dipartimento di Ingegneria e Fisica dell'Ambiente, Università della Basilicata, viale dell'Ateneo Lucano n. 10, 85100 Potenza, Italy

²Goddard Earth Sci. and Technology Center, Univ. of Maryland Baltimore County, MD, USA

³Mesoscale Atmospheric Processes Branch, NASA GSFC, Code 613.1 Building 33, Greenbelt, MD 20771, USA

⁴Dipartimento di Fisica, Università di Bologna, viale Berti-Pichat 6/2, 40127 Bologna, Italy

Received: 8 June 2009 – Published in Atmos. Chem. Phys. Discuss.: 8 July 2009

Revised: 31 October 2009 – Accepted: 2 November 2009 – Published: 19 November 2009

Abstract. Raman lidar measurements performed in Potenza by the Raman lidar system *BASIL* in the presence of cirrus clouds are discussed. Measurements were performed on 6 September 2004 in the frame of the Italian phase of the EAQUATE Experiment.

The major feature of *BASIL* is represented by its capability to perform high-resolution and accurate measurements of atmospheric temperature and water vapour, and consequently relative humidity, both in daytime and night-time, based on the application of the rotational and vibrational Raman lidar techniques in the UV. *BASIL* is also capable to provide measurements of the particle backscatter and extinction coefficient, and consequently lidar ratio (at the time of these measurements, only at one wavelength), which are fundamental to infer geometrical and microphysical properties of clouds.

A case study is discussed in order to assess the capability of Raman lidars to measure humidity in presence of cirrus clouds, both below and inside the cloud. While air inside the cloud layers is observed to be always under-saturated with respect to water, both ice super-saturation and under-saturation conditions are found inside these clouds. Upper tropospheric moistening is observed below the lower cloud layer.

The synergic use of the data derived from the ground based Raman Lidar and of spectral radiances measured by the NAST-I Airborne Spectrometer allows the determination of the temporal evolution of the atmospheric cooling/heating rates due to the presence of the cirrus cloud.

Lidar measurements beneath the cirrus cloud layer have been interpreted using a 1-D cirrus cloud model with explicit microphysics. The 1-D simulations indicate that sedimentation-moistening has contributed significantly to the moist anomaly, but other mechanisms are also contributing. This result supports the hypothesis that the observed mid-tropospheric humidification is a real feature which is strongly influenced by the sublimation of precipitating ice crystals. Results illustrated in this study demonstrate that Raman lidars, like the one used in this study, can resolve the spatial and temporal scales required for the study of cirrus cloud microphysical processes and appear sensitive enough to reveal and quantify upper tropospheric humidification associated with cirrus cloud sublimation.

1 Introduction

Cirrus clouds represent a fundamental component of the global climate system, primarily through their radiative effects (Liou, 1986; Stephens et al., 1990). Cirrus radiative properties are important modulators of the incoming solar and the outgoing planetary radiation (Ramanathan et al., 1983). A proper understanding of the formation mechanisms of cirrus clouds in the upper troposphere and tropopause region is a necessary prerequisite to understand and predict the radiative effects of cirrus clouds, their role in precipitation processes and in the hydrological cycle, and hence their impact on climate.

The role played by cirrus clouds in humidifying the underlying atmosphere through evaporation of falling ice crystals is important. The associated pattern of evaporative cooling



Correspondence to: P. Di Girolamo
(paolo.digirolamo@unibas.it)

may act to significantly alter the pre-existing static stability in the sub-cloud region and, together with a humidification effect, may ultimately result in the formation of new cloud layers (Starr and Wylie, 1990). Furthermore, crystals precipitating from cirrus clouds can seed lower super-cooled liquid water clouds and influence precipitation mechanisms (Ramaswamy and Detwiler, 1986). Upper tropospheric humidification has important climatic implications as climate sensitivity to increasing CO₂ is primarily dependent on water vapour feedback mechanisms taking place in the middle and upper troposphere (Sinha and Harries, 1995; Held and Soden, 2000).

This paper aims to show the capabilities of Raman lidar systems in the characterization of atmospheric processes involving cirrus clouds. Measurements reported in this paper were performed in the frame of the Italian phase (5–10 September 2004) of the European AQUA Thermodynamic Experiment (EAQUATE) (Taylor et al., 2008). The experiment involved also a variety of ground based remote sensing instruments (lidars, microwave radiometer, infrared interferometer, ceilometer), and was supported by dedicated radiosonde releases from the IMAA-CNR ground station 8.2 km away, in the W-SW direction. The University of BASILicata UV Raman lidar system (*BASIL*), located at the Dipartimento di Ingegneria e Fisica dell'Ambiente (DIFA) in Potenza-Italy (40°38'45" N, 15°48'32" E), was part of the ground equipment involved in the experiment and collected approximately 80 h of measurements distributed over four Intensive Observation Periods (IOPs). The NASA Proteus high altitude aircraft provided measurements through a range of instruments, and among them the National Polar-orbiting Operational Environmental Satellite System (NPOESS) Airborne Sounder Testbed-Interferometer (NAST-I), a scanning sensor measuring emitted thermal radiation with a spectral resolution of 0.25 cm⁻¹, covering the long wave band region 645–2700 cm⁻¹ (Cousins and Gazarick, 1999).

NAST-I measurements were compared with spectral radiances computed using *BASIL* products (temperature and water vapour profiles, and cloud geometrical and optical information) leading to the determination of the temporal sequence of the cloud cooling/heating rates associated with the presence of the cirrus cloud (more details on the approach are provided in section 3). Lidar measurements beneath cirrus clouds have been interpreted using a 1-D cirrus cloud model with explicit microphysics.

The paper outline is as follows. Section 2 describes the Raman lidar system and the meteorological conditions at the time of the measurements and illustrates the lidar measurements in the presence of the cirrus clouds. Section 3 describes the methodology used to estimate the cooling/heating rates generated by the cirrus cloud. Section 4 describes the cirrus cloud microphysical model and the results of the cloud simulations used in the interpretation of the lidar measurements. Results are summarized in Sect. 5.

2 The case study: lidar system and measurements

The major feature of *BASIL* is represented by its capability to perform high-resolution and accurate measurements of atmospheric temperature and water vapour, both in daytime and night-time, based on the application of the rotational and vibrational Raman lidar techniques in the UV (Di Girolamo et al., 2004, 2009). Relative humidity measurements are obtained from the simultaneous lidar measurements of water vapour and temperature. Lidar measurements of atmospheric temperature and water vapour reported in this paper were calibrated by comparing *BASIL* products with radiosonde measurements of these same parameters for the 17 radiosonde released from the IMAA-CNR ground station during the EAQUATE experiment. The altitude regions considered for the comparison were chosen to be 3–7 km above mean sea level (a.s.l.) for water vapour and 5–10 km a.s.l. for temperature. From now on all references to height or altitude are intended as a.s.l., unless otherwise noted. Vibrational and rotational Raman lidar techniques for the measurement of atmospheric humidity and temperature and the methodologies used for the data analysis are described in a variety of papers (among others, Whiteman et al., 2006a,b; Behrendt and Reichardt, 2000; Ferrare et al., 2004; Di Girolamo et al., 2006; Behrendt, 2005). When particle scattering ratios are in excess of 45 (Behrendt and Reichardt, 2000), lidar temperature measurements are contaminated by elastic echoes. This potential source of systematic error is minimized through the application of a correction algorithm based on the knowledge of the intruded elastic signal, which is subtracted from the temperature signals.

Besides temperature and water vapour, at the time of this experiment *BASIL* provided measurements of particle backscattering and extinction coefficient at 355 nm, both in daytime and night-time. The experimental set-up of *BASIL* is described in several other papers (Maestri et al., 2009; Bhawar et al., 2008; Griaznov et al., 2007; Mona et al., 2007; Di Girolamo et al., 2009). Vertical and temporal resolution of *BASIL* raw data are 30 m and 1 min, respectively. However, in order to reduce signal statistical fluctuations, time integration and vertical smoothing are applied to the data. For a time integration of 10 min and a vertical resolution of 300 m, night-time measurement uncertainty at 8 km a.s.l. is typically 5% for the particle backscattering coefficient, 20% for particle extinction coefficient, 6% for water vapour mixing ratio, 0.5 K for temperature and 4% for RH.

On 6 September 2004 the cirrus cloud evolution was monitored by *BASIL* between approx. 17:30 and 20:30 UTC in the altitude region from 7 to 11 km a.s.l. The Proteus aircraft flew four times over the Potenza region and three radiosondes were released in 4 h from the IMAA ground station.

In the morning intense convective activity was present over Molise, Northern Campania and Basilicata mainly along the Appennines, NW of Potenza (see the sequence of SE-VIRI images at 10.8 μm (channel IR108) and at 6.25 μm

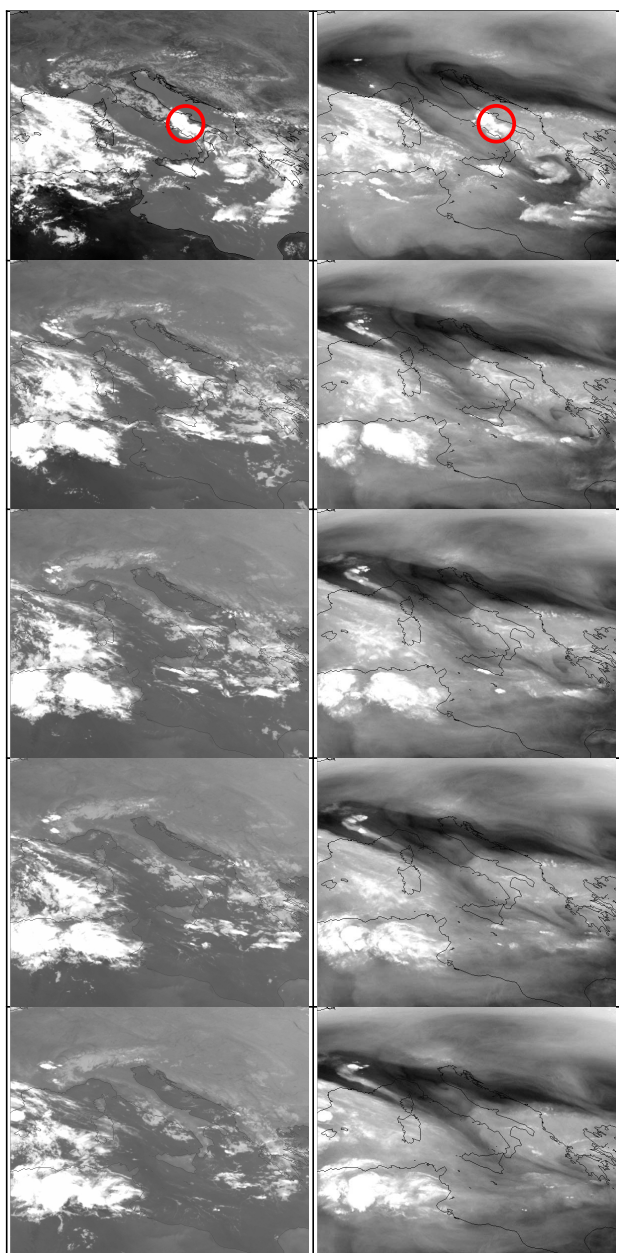


Fig. 1. Sequence of images from MSG SEVIRI: channel IR108 (centered at $10.8\ \mu\text{m}$) on left column and channel WV62 (centered at $6.25\ \mu\text{m}$) on the right column. The figures cover the latitude range from $30^\circ\ \text{N}$ to $48^\circ\ \text{N}$ ($\sim 2000\ \text{km}$) and the longitude range from $0^\circ\ \text{E}$ to $22^\circ\ \text{E}$ ($\sim 2300\ \text{km}$). The timing (from top to bottom) is: 13:12:44, 17:12:45, 18:42:44, 19:42:43 and 21:27:43 UTC. In the images for 13:12:44 the region where intense convective activity was present in the morning hours (Molise, Northern Campania and Basilicata) is marked with red circles.

(channel WV62) in Fig. 1). SEVIRI images in the WV62 water vapour channel show that the convective activity took place at the border of an area of relatively high humidity slowly drifting South East, limited to the West by a region of drier air moving quickly South-East over the Tyrrhenian

Sea and the island of Sicily. Low and mid level clouds were completely dissipated around 17:30 UTC, while a persistent cirrus cloud, of limited extent and primarily located E of Potenza, is visible at 18:42 UTC until 21:27 UTC. The complete sequence of SEVIRI images in the infrared and water vapour channels (not shown) indicates that the air mass where the main convective activity had taken place kept moving South East, over the Potenza region, at an estimated average speed (computed considering persistent high-cloud features) of less than $10\ \text{m/s}$, much lower than the speed of the drier air-mass on the Tyrrhenian Sea and the island of Sicily (about $20\text{--}30\ \text{m/s}$).

Figure 2 shows the variability of the particle backscattering coefficient at $355\ \text{nm}$ over the period 17:32–20:34 UTC, clearly revealing the evolution of the cirrus cloud episode till final dissipation. The figure is plotted as a succession of 1 min averaged consecutive profiles and covers the day-to-night transition. No lidar data are available before 17:30 UTC; however, before this time, the large cloud optical thickness and sky background radiation would have prevented accurate lidar measurements from inside cirrus clouds, especially in terms of water vapour mixing ratio.

Cloud boundaries are determined through the application of a threshold approach (Platt et al., 1994). A threshold value of $2.5 \times 10^{-7}\ \text{m}^{-1}\ \text{sr}^{-1}$ is considered to infer cloud base and top height (cloud boundaries are illustrated with a bold black line in Fig. 2). The cloud deck is well distinguishable in the figure till approximately 19:20 UTC and afterwards the presence of a residual cloud signature is visible between 19:45 and 20:30 UTC. Two cloud layers are present: a lower layer extending from 7.3 to 9.6 km and vanishing around 18:30 UTC, and an upper layer extending from 9.2 to 10.7 km, present till 20:30 UTC. The vertical extent of the cloud is found to progressively decrease with time, with a maximum value of 3.5 km around 18:00 UTC. Detailed information on the time variability of the geometrical and optical properties of the cirrus cloud for this specific case study have been reported in other papers (Mona et al., 2007; Maestri et al., 2009).

Figure 3 shows the lidar measurements of particle extinction at $355\ \text{nm}$ over the same 3 h period as in Fig. 2, plotted as a succession of 1 min averaged consecutive profiles. Particle extinction measurements are independent from particle backscatter measurements, as the former are obtained from the N_2 Raman lidar signals at $386.7\ \text{nm}$ (Ansmann et al., 1992), while the latter are obtained from the elastic lidar signals at $355\ \text{nm}$. In order to reduce signal statistical fluctuations, vertical smoothing is applied to the raw N_2 Raman signals to achieve an overall vertical resolution of $150\ \text{m}$. Extinction measurements are however not sensitive enough to capture the cloud signature between 19:45 and 20:30 UTC. Figure 3 also shows the evolution with time of cloud optical thickness τ (lower panel), obtained by integrating the extinction profiles over the vertical domain of the clouds ($7\text{--}12\ \text{km}$), through the expression:

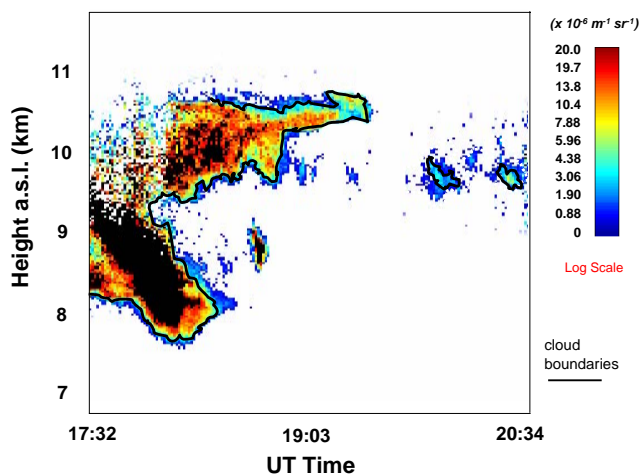


Fig. 2. Time evolution of particle backscattering coefficient at 355 nm from 17:32 to 20:34 UTC on 6 September 2004. Here and in the following figures, height is expressed in km above mean sea level (a.s.l.).

$$\tau = \int_{z_1}^{z_2} \alpha(z) dz \quad (1)$$

with $\alpha(z)$ being the particle extinction profile, and z_1 and z_2 being the lower and upper integration limit (in this case 7 and 12 km, respectively).

Optical thickness ranges from 2.76, at 18:02 UTC, to 0.01, at 19:30 UTC. It is to be pointed out that the laser beam gets completely extinguished when the optical thickness is exceeding 2.8–3. Therefore, it is possible that optical thickness values in excess of 3 are present before 18:00 UTC, but the system cannot obtain a correct estimate of them. From the simultaneous lidar measurements of particle extinction and backscatter the lidar (extinction-to-backscatter) ratio at 355 nm is obtained. The lidar ratio depends on particle microphysical properties, primarily particle size and shape. Values are in the range 25–30 sr, which are in good agreement with other literature values for cirrus cloud particles (Behrendt and Reichardt, 2000; Chen et al., 2002; Gianakaki et al., 2007). A more detailed analysis of lidar ratio variability for this case study has been reported in a recent paper by Mona et al. (2007).

Figure 4 illustrates the time evolution of the relative humidity over ice (RHI), computed using the saturation vapour pressure over ice. The figure is plotted as a succession of consecutive profiles (averaged over a 5 min period), and vertical resolution is 300 m. Cloud boundaries are shown in this figure (white lines), together with the maximum altitude (red line) reached for water vapour mixing ratio lidar measurements, which is taken as the altitude where the random component of the error affecting water vapour mixing ratio measurements reaches 100%. Because of the severe attenuation of the laser beam by the cloud, penetration of water vapour measurements inside cirrus clouds is limited to a total optical

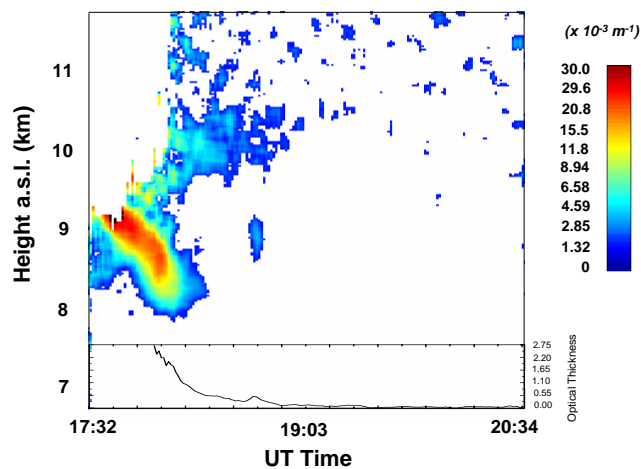


Fig. 3. Time evolution of the particle extinction coefficient (same time-frame as Fig. 2). The lower panel shows the evolution with time of total cloud optical thickness.

thickness of about 2.5–3. For cloud regions where scattering ratio exceeds 30, RHI is computed using the temperature information from four radiosondes that were released at 17:13, 18:36, 20:22 and 00:32 UTC from the IMAA-CNR ground station. For this purpose, radiosondes data are interpolated at the times and heights of the lidar data. Results plotted in Fig. 4 show that both super-saturation and under-saturation conditions (with respect to ice) are found inside the cloud. Additionally, values of RHI in excess of 100% are found beneath the cirrus clouds (see regions identified with blue arrows in Fig. 4). Some of these values, especially those observed above 10 km, are due to the large statistical noise affecting the lidar data.

In order to compare vertical profiles of particle backscatter, relative humidity and temperature at a fixed time, we considered a 10 min average identified by the vertical red line in Fig. 4, covering the time interval 19:05–19:15 UTC. Corresponding profiles are illustrated in Fig. 5. This time was selected in order to minimize the temporal mismatch between radiosonde and lidar measurement at cirrus altitude. In fact, in the time interval 19:02–19:12 UTC the radiosonde launched at 18:36 is found to cover the altitude region 7.7–10.4 km.

In panel (a) of Fig. 5, the black line represents the lidar profile of relative humidity over water (RH), the red line is the lidar profile of RHI and the green line is the radiosonde profile of RH. The particle backscatter profile at 355 nm is illustrated in panel (b). Note that values of RH and RHI measured by *BASIL* are found to noticeably increase inside the cirrus cloud, while the radiosonde values of RH do not. Although the radiosonde was not equipped with a GPS receiver for absolute positioning, wind information from the ECMWF global model suggests that, at the time of the lidar measurement, the radiosonde is within a distance of 12 km from the

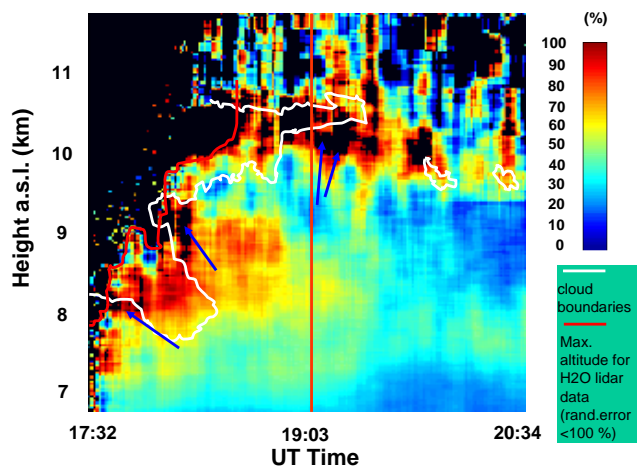


Fig. 4. Time evolution of RHI on 6 September 2004. White lines represent cloud boundaries, while red lines represent the maximum reached altitude for water vapour lidar measurements. The red vertical line identifies the 10 min average profiles (19:05–19:15 UTC) considered in Fig. 5. Large relative humidity values beneath the clouds (blue arrows) are associated with upper tropospheric humidification caused by the sublimation of precipitating ice crystals.

measurement site. SEVIRI satellite images at 18:57:45 UTC and 19:12:45 UTC show that cloud coverage extends over an area of several hundred km² around Potenza. Therefore we think that the radiosonde RH profile inside the cloud layer is likely due to the slow response time of the radiosonde humidity sensor (advanced humicap for the Vaisala RS-90A) rather than to a drift away from the area covered with cirrus clouds. Panel (c) and (d) of Fig. 5 represent a magnification of the region 9–11 km of panel (a) and (b), respectively, while panel (e) represents the temperature profile in this same altitude region. Large RHI values in excess of 120% are observed within the cirrus cloud layer. Very large RHI values, up to 160%, have been reported by several authors (e.g. Gierens et al., 1999; Ovarlez et al., 2002; Ström et al., 2003). Panel (c), (d) and (e) reveal that both RH and RHI within the cloud increase with decreasing temperatures. Additionally, the fraction of the cloud volume which is under-saturated with respect to ice decreases with height. These results are in agreement with other in situ observations in ice clouds (Kolorev and Isaac, 2006).

Figure 6 illustrates the time evolution of water vapour mixing ratio over a time period of approx. 9.5 h from 17:32 UTC on 6 September 2004 to 02:55 UTC on 7 September 2004. The figure is plotted as a succession of 10 min averaged consecutive profiles with a vertical resolution of 300 m; this large integration time was selected in order to reduce random errors. Additionally, in order to clearly highlight the elevated humid layer in the 6–8 km altitude range, the colour scale was selected to range between 0 and 2 g/kg. The layer of increased humidity beneath the cloud layer appears as a horizontal stripe in the altitude range from 6 to 7.5 km, included

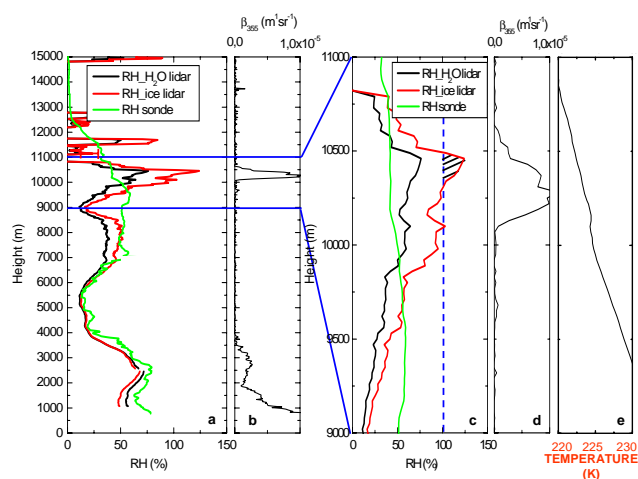


Fig. 5. 10 min average profiles for the time interval 19:05–19:15 UTC: (a) lidar profiles of RH (black line) and RHI (red line) and radiosonde profile of RH (green line); (b) particle backscatter profile at 355 nm; (c) magnification of panel (a) in the vertical region the 9–11 km (a.s.l.); (d) magnification of panel (b) in the vertical region the 9–11 km; (e) lidar profile of atmospheric temperature in the vertical region the 9–11 km.

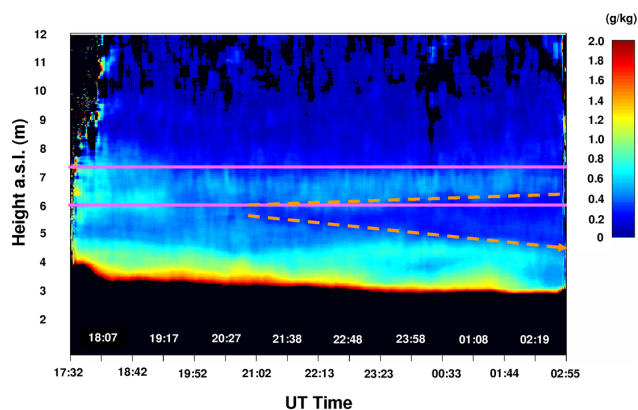


Fig. 6. Time evolution of water vapour mixing ratio over the time period of approx. 9.5 h from 17:32 UTC on 6 September 2004 to 02:55 UTC on 7 September 2004. A humid layer is present between 6 and 7.5 km a.s.l. (included between the two horizontal violet lines).

between the two horizontal violet lines. Before 19:20 UTC, *BASIL* is sounding an air column which includes the cirrus cloud (see Fig. 2 for comparison) and the high water vapour mixing ratio values observed before 19:20 UTC pertain to humid air masses inside the lower portion of the cloud layer.

At the beginning of this section, information concerning the typical values of precision for the different atmospheric parameters measured by *BASIL* was provided. However, this information refers to clear-sky, night-time operation at a specified altitude, based on nominal laser power and consequently a more detailed assessment is required for

the results reported in this study, with a specific reference to the measurements performed in terms of water vapour mixing ratio and RHI in the altitude region 5–11 km, inside and beneath the cirrus clouds, both at night and in the dusk-to-night transition period, considering the specific system performances on that day. This can be easily achieved as the statistical uncertainty affecting lidar measurements can be analytically estimated from the measured lidar signals through the application of Poisson statistics, which is well suited in cases of data acquired in photon-counting mode, as in the case of *BASIL*. Results shown in Fig. 7 (obtained considering a vertical and temporal resolution of 300 m and 10 min, respectively) reveal that water vapour mixing ratio measurements are affected by a percent random error, $\Delta x_{\text{H}_2\text{O}}(z)/x_{\text{H}_2\text{O}}(z)$, at night (19:00 UTC) smaller than 2% up to 5.5 km, smaller than 5% up to 7.5 km and not exceeding 25% up to 10.5 km. For operation in the dusk-to-night transition period (18:00 UTC), $\Delta x_{\text{H}_2\text{O}}(z)/x_{\text{H}_2\text{O}}(z)$ is smaller than 10% up to 5.5 km, smaller than 25% up to 7.5 km and does not exceed 100% up to 10.5 km. The random error for relative humidity measurements, $\Delta \text{RH}(z)$, at night is smaller than 1.5% up to 5.5 km, smaller than 3.5% up to 7.5 km and smaller than 6.5% up to 10.5 km. For operation in the dusk-to-night transition period, $\Delta \text{RH}(z)$ is smaller than 3% up to 5.5 km, smaller than 7.5% up to 7.5 km and smaller than 12% up to 10.5 km.

3 Estimate of radiative diabatic exchange

The NAST-I measurements in the window region 10–12 μm were used to retrieve total cloud optical depth and effective dimension D_e using the method RT-RET (Maestri and Holz, 2009). Surface emissivity of the Potenza region is derived from SSEC (Space Science and Engineering Center, University of Wisconsin-Madison, USA) gridded dataset (Borbas et al., 2007), using a baseline fit method on MODIS (The Moderate Resolution Imaging Spectroradiometer) surface emissivity retrieval algorithm (MOD11). As surface skin temperature we considered the lowermost atmospheric temperature value obtained from the radiosonde since a direct measurement was not performed and retrievals from remote sensing data were prevented by the cloudy sky. Several retrievals have been obtained using various particle habits and specific analytic Gamma functions to describe the particle size distribution (PSD) (more details are given in Sect. 4). The best results, measured by the closeness of the simulated and measured spectral radiances, are obtained assuming a prescribed mixture of crystal habits (Bozzo et al., 2008). Table 1 lists the optical and microphysical properties retrieved by RT-RET at 4 field-of-views (FOVS) around the *BASIL* station, during the first Proteus overpass, assuming the mentioned mixture. The results for the four closely spaced NAST-I FOVS are given to show the small-scale variability in retrieved cloud optical thickness, and therefore the range expected for the mi-

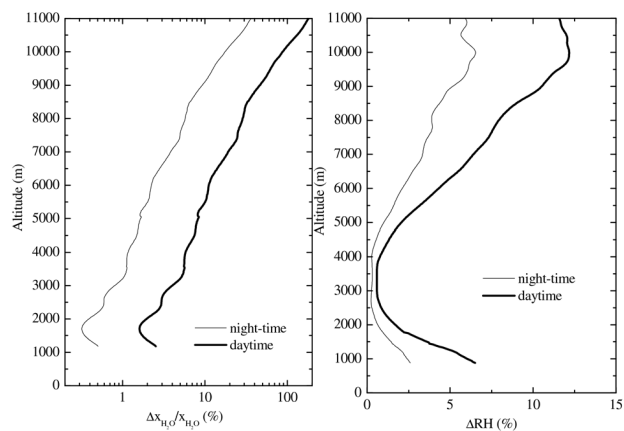


Fig. 7. Random error affecting water vapour mixing ratio (left panel, expressed in percentage) and relative humidity (right panel) measurements by *BASIL* at night (19:00 UTC on 6 September 2004) and for operation in the dusk-to-night transition period (18:00 UTC on 6 September 2004). Precision estimates are based on a vertical and temporal resolution of 300 m and 10 min, respectively.

crophysical parameters. Table 1 also provides values corresponding to the average properties over the four FOVS, computed from the average radiances. These mean properties are used for the simulations presented in this section. The estimate of D_e is representative of the whole cloud deck, which is a reasonable assumption in this case study since the measured lidar ratio is nearly constant within the cloud deck.

The retrieved effective dimension D_e is then used to compute the mean extinction coefficient k_e [m^2/kg] valid for the entire cloud deck, using same hypothesis on PSD and shape used for the retrieval step. Finally the mass density profile $\rho(z)$ [kg/m^3], also called Ice Water Content, or IWC, can be derived in any layer where lidar measurements of the extinction coefficient β_e [m^{-1}], are available, using the expression:

$$\rho(z) = \frac{\beta_e(z)}{k_e} \quad (2)$$

The main underlying assumption, as already pointed out, is that the particle size distribution, and hence the effective dimension, does not change throughout the cloud. This assumption is confirmed by the lidar ratio measurements, which show a limited variability inside the cloud (within the range 25–35 sr), this variability being comparable to the noise error affecting the estimate of the mean lidar ratio inside the cloud (29 ± 4 sr).

Thus a synergistic use of lidar and NAST-I derived parameters allows a reconstruction of all the quantities that are needed for simulating the upwelling radiances in cloudy conditions. This procedure has been applied to four closely spaced sets of FOVS closest to the *BASIL* line of sight for each of the Proteus overpasses (four in all) over the DIFA ground station. The average microphysical properties retrieved using RT-RET and Raman lidar measurements

Table 1. Optical and microphysical properties retrieved from the RT-RET retrieval scheme during the first Proteus overpass at 18:02 GMT (Maestri et al., 2009), assuming a mixture of crystal habits. L and μ are the so called “slope” and “dispersion” parameters of the PSD and $D_e = \frac{3\int N(D)VdD}{2\int N(D)AdD}$, is the effective diameter, where V is the volume and A is the projected area. The table also reports the values corresponding to the average properties over the four FOVS, computed from the mean radiance.

NAST-I FOV number	Shortwave optical depth	Longwave optical depth	L cm^{-1}	μ	D_e micron
1	1.7	1.6	328	7	60
2	2.3	2.2	242	7	72
3	2.7	2.5	242	7	72
4	2.1	2.0	416	7	52
average	2.2	2.1	307	7	64

of atmospheric temperature, water vapour, cloud geometry (cloud upper and lower boundaries) and mass density profile $\rho(z)$ [kg/m^3], have been used for the radiative transfer (RT) computations at the time of the Proteus passes. Multiple scattering RT calculations are performed using the adding and doubling method (Evans and Stephens, 1991). The RT code is interfaced with the molecular optical depth database, obtained using LbLRTM (Clough and Jacono, 1995) and the particulate optical depth database as described in Rizzi et al. (2001) and Maestri et al. (2005). The detailed comparison of the four sets of NAST-I data with our simulations can be found in Maestri et al. (2009). As the simulated radiances are in good agreement with measured NAST-I data, we expect that the reconstruction of the relevant atmospheric and cloud parameters is good enough to allow the reconstruction of the temporal evolution of the atmospheric fluxes and thus of the radiative diabatic terms, that can be expressed in terms of the cooling/heating rates, and to investigate the energy balance at the time of observations.

Spectral fluxes and cooling/heating rates have been computed in coincidence with the four NAST-I overpasses with a resolution of 0.05 cm^{-1} . Corresponding spectral cooling/heating rates are shown in Fig. 8, where the spectral resolution has been degraded to 20 cm^{-1} for visual purposes. During the first overpass (18:02 UTC, upper left panel) the cloud is formed of two optically thick layers with a similar optical depth (OD) (1.62 for the lower layer and 1.14 for the upper layer, values obtained by integrating the lidar extinction coefficient over the depth of the two layers). These high optical depth values generate heating at cloud base in the window region, while in the far infrared the cloud base is immersed in a quite opaque environment dominated by the water vapour absorption in the rotational band, which leads to very low heating/cooling rate values. Maximum cooling is

observed at the cloud top between 200 and 600 cm^{-1} . During the second overpass (18:20 UTC, upper right panel) the lower cloud layer has almost disappeared (OD=0.06 for the lower layer and 0.64 for the upper layer) and the window heating and far infrared cooling take place at the cloud top. A similar situation is found during the third overpass (19:20 UTC, lower left panel), but lower heating and cooling rates are present as a result of smaller optical depth (OD=0.03 for the lower layer and 0.14 for the upper layer).

During the fourth overpass (19:40 UTC, lower right panel) the typical features of the clear sky cooling rates are present (overall OD=0.06). The main diabatic feature is represented by the cooling structure of the water vapour rotational band between 2–4 km a.s.l. in the spectral region $400\text{--}600 \text{ cm}^{-1}$, a feature not present during the first overpass in the presence of strong down-welling fluxes due to the cloud layers.

Spectral cooling/heating rates can be spectrally integrated to determine the vertical profiles of total diabatic rates, which are plotted in Fig. 9 for the four Proteus overpasses. During the first overpass, the cloud effect is evident both inside and outside the cloud layers. A large gradient ($\sim 10 \text{ K}/\text{day}$) develops between cloud top and bottom. The strong cooling at the top during the first overpass can explain the persistence of the upper cloud layer after 19:00 UTC, when the lower portion has already disappeared. During the second overpass, as a result of the almost complete disappearance of the lower cloud layer, the window heating and far IR cooling occur at approximately the same altitude and nearly compensate each other, thus producing a reduced cooling at the top of the cloud. The disappearance of the cloud cannot be explained based on radiative energy exchange mechanisms alone, and cloud microphysics needs to be accounted for. We have therefore relied on a 1-D microphysical model to describe the evolution of the cloud, starting from initial conditions which represent the measured state over Potenza at 17:32 UT. The details of the 1-D model are introduced in the next section, together with the obtained results.

4 Cloud simulations

The one-dimensional (1-D) time-dependent cloud numerical model with explicit microphysics (Lin et al., 2005) is capable of fully resolving the PSD in each grid box. Ice crystals are grouped into bins according to their ice masses to resolve the evolution of the PSD. One-dimensional simulations of anvil clouds have been explored by several authors (e.g. Chen et al., 1997). The most sophisticated 1-D cloud simulation would be using a framework of single column model (e.g. Luo et al., 2003; Comstock et al., 2008), given the horizontal moisture and heat flux, or even the horizontal flux of condensate. The soundings indicate that the horizontal wind in the mid-upper troposphere (5–9 km) was light for the period of interest for this study; the sequence of infrared and water vapour MSG imagery shows that the air mass in

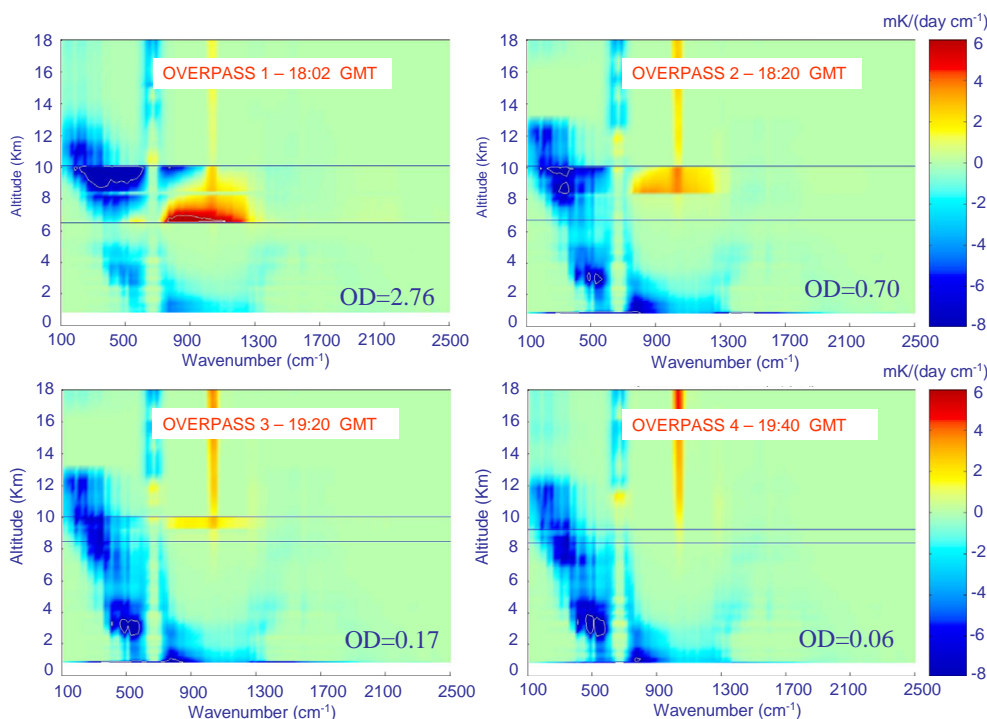


Fig. 8. Spectral cooling/heating rate profiles in correspondence of the 4 Proteus overpasses over *BASIL*. The time sequence is 1st overpass: upper left, 2nd overpass: upper right, 3rd overpass: lower left and 4th overpass: lower right panel. In the 4 panels the lidar measured cloud optical depths (in the short-wave) are also reported. Altitude in km (from 0 to 18) a.s.l. is reported on Y-axis and wave number (from 100 to 2500 in cm^{-1}) on X-axis. For visual purposes, spectral cooling/heating rates are averaged on a spectral window of 20 cm^{-1} .

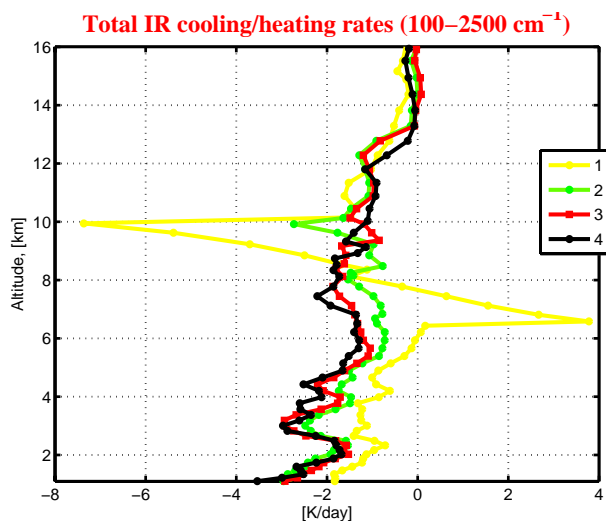


Fig. 9. Vertical profiles of total infrared cooling/heating rates in correspondence of the 4 Proteus overpasses over *BASIL*.

which the cloud is embedded moves slowly toward South-East, and moreover water vapour imagery (both at 6.2 and $7.3 \mu\text{m}$) shows that the same air mass is fairly horizontally homogeneous. Because of the limited horizontal advection, the cirrus cloud progressively vanishes mainly as a result of

radiative diabatic heating, mesoscale induced downward motion and particle fall-out and sublimation. The radiative diabatic terms computed in Sect. 3 support an important diabatic effect at the time of the first Proteus pass only, while at later stages the only radiative effect is seen as a moderate cooling of the top of the upper layer.

The initial conditions for the 1-D simulation are the idealized profiles of temperature and vapour mixing ratio shown in Fig. 10, obtained from the radiosonde data at 17:13 UTC. The use of the radiosonde data to initialize the model became necessary because, due to signal attenuation and noise problems, the full profile of temperature and water vapour mixing ratio from Raman lidar was not obtained until 18:22 UTC. The actual radiosonde profiles at 17:13 and 18:36 UTC are also plotted in the same figure for comparison. In the altitude range of interest (5–11 km) there is a warming trend in potential temperature, except at $z=7$ km and $9 < z < 10$ km. Take the air at 7.5 km for example, where the potential temperature increases by 0.55 K from 17:13 to 18:36 UTC. This corresponds to a downward motion of 0.055 ms^{-1} , ignoring the horizontal heat advection and any diabatic heating. In both soundings, RHI is less than 40% between $z=5$ and 5.8 km and increases with height to 100% at around $z=7.2$ km. RHI for the two soundings differ significantly between $z=7.2$ and 8.8 km: at 17:13 UTC RHI is mostly ice supersaturated whereas at 18:36 UTC it is mostly undersaturated. It

is conjectured that this change in RHI is associated with a mesoscale-induced descending air motion superimposed with gravitational settling of ice particles. RHI in both soundings is close to ice saturation between 8.8 and 9.8 km and decreases with height above 9.8 km. For simplicity, RHI is set to 100% between 7.2 and 9.8 km for the idealized profile used as initial condition for the simulation.

As previously mentioned, *BASIL* measurements show that the cirrus cloud gradually split into two layers and the lower layer is completely detached from the top one from around 18:00 UTC (Fig. 2). The base of the lower layer descended from $z=8.8$ km at 17:32 UTC to $z=7.6$ km at 18:12 UTC, while the upper layer top height did not change much from the beginning of the lidar measurement till its final disappearance (19:30 UTC). The deepening of the cloud-free region between the two layers took place concurrently with a gradual reduction in RHI (Fig. 4).

In what follows we examine to what extent the observed evolution of RHI and extinction profiles, measured by *BASIL*, is compatible with the evolution predicted by the 1-D model with horizontal advection terms ignored. Note that the purpose of cloud simulations is to examine whether our hypothesis (of upper tropospheric humidification associated with sublimation of precipitating ice crystals) is realistic, given the data available. Ice particle sedimentation and sublimation in ice sub-saturated environment is a mechanism capable to redistribute water vapour mass vertically. The 1-D model results are postprocessed to compute how much ice mass is converted to water vapour mass as a function of height. Cirrus cloud particles are assumed to be hexagonal columns, so that their length and diameter relationship follows Eqs. (8) and (9) of Mitchell and Arnott (1994), and their size is described by a Gamma size distribution of the type:

$$N(D) = N_0 D^\mu \exp(-LD) \quad (3)$$

with D being the cloud particle maximum dimension, N_0 being the intercept value of the distribution, L being the inverse of the characteristic dimension, and μ being the shape parameter controlling the width of the distribution. The initial PSD profile is derived using the microphysical properties retrieved from NAST-I using RT-RET, as described in Sect. 3, but using hexagonal columns, and the particle backscatter profile measured by the Raman lidar at 17:32 UTC.

The retrieved parameters L and μ are then used to obtain the profile of N_0 by the following procedure: given that the measured lidar ratio is about 25 sr then $\beta_e \approx 25\beta_s$, where $\beta_e = \int N(D) A Q_e dD$ and β_s are the particle extinction coefficient and the backscattering coefficient, respectively; A is the projected area of the particle, and Q_e is the extinction efficiency. Therefore

$$N_0 = \frac{25\beta_s}{\int D^\mu \exp(-LD) A Q_e dD} \quad (4)$$

To obtain N_0 , it is further assumed that (1) particles are randomly oriented so that the projected area is one quarter of

the surface area; (2) $Q_e=2$. The retrieved profile of the particle number concentration ($N_{\text{ice}} = \frac{N_0(\mu+1)}{L^{\mu+1}}$) is plotted in Fig. 10d. The plot shows that roughly a factor of two difference in N_{ice} would result from the change of L from 206 to 326 cm^{-1} , values which reflect the range of values retrieved, assuming hexagonal columns, in the four NAST-I FOVS during the first Proteus overpass.

The 1-D model considers 60 equally-spaced height levels, from 5 km to 11 km. The starting time of the simulation is 17:32 UTC. Simulation time is 120 min and the time step is 5 s. As described in the previous paragraphs, the time evolution of potential temperature and RH_{ice} indicate that air might have been descending, at least between 7 and 9 km. Therefore, a uniform downward vertical velocity of 0, -0.05 , -0.1 , -0.15 and -0.20 ms^{-1} is prescribed in the vertical domain of interest.

The results of the simulations are plotted in Fig. 11. The simulations capture the descending lower cloud layer reasonably well in the first 30 min (17:32 to 18:02 UTC), especially those simulations using a faster downward vertical velocity. Furthermore, simulations using $L=206$ are slightly better than those using $L=326$. The lidar observation indicates that the lower cloud layer thins rather quickly between 18:02 and 18:12 UTC (Fig. 3). In contrast, none of the simulations captures the abrupt thinning. Given the temperature and RHI of the cloud deck, the observed fast thinning was more likely caused by horizontal advection of the air and cloud than by particle sublimation. Evidently from the Fig. 11a and b, the simulations miss capturing the evolution of the upper cloud layer which might be due to the following reasons: (1) the specification of a uniform downward vertical velocity throughout the entire model domain; (2) the use of a unimodal gamma size distribution that might have underestimated the number of small particles for the initial PSDs; (3) not accounting for the radiative diabatic effects and (4) the lack of exact co-location of synergistic measurements from lidar, radiosondes and NAST-I.

The simulations are able to capture the basic features of the water vapour mixing ratio and RHI profiles (Fig. 11c–f). The result is moderately affected by the assumed characteristic length ($1/L$) for the given range ($206 \leq L \leq 326 \text{ cm}^{-1}$). Note that we don't recommend the use of Fig. 11 to infer the vertical speed for this case because the humidity measurements by lidar show large amplitude fluctuations in the mid-troposphere, suggesting horizontal moisture advection. Furthermore, although the radiosondes at 17:13 and 18:32 UTC seem to indicate a gentle downward motion, the true downward motion could be larger and fluctuating with time, as shown in some cirrus observations (Comstock et al., 2008).

There are at least 3 issues that need to be addressed in order to verify our working hypothesis: does the cirrus cloud moisten that layer ($6.5 < z < 7.5$ km)? How much vapour mass does the cirrus contribute to that layer? Is the observed moist anomaly in mixing ratio profiles due to sedimentation-

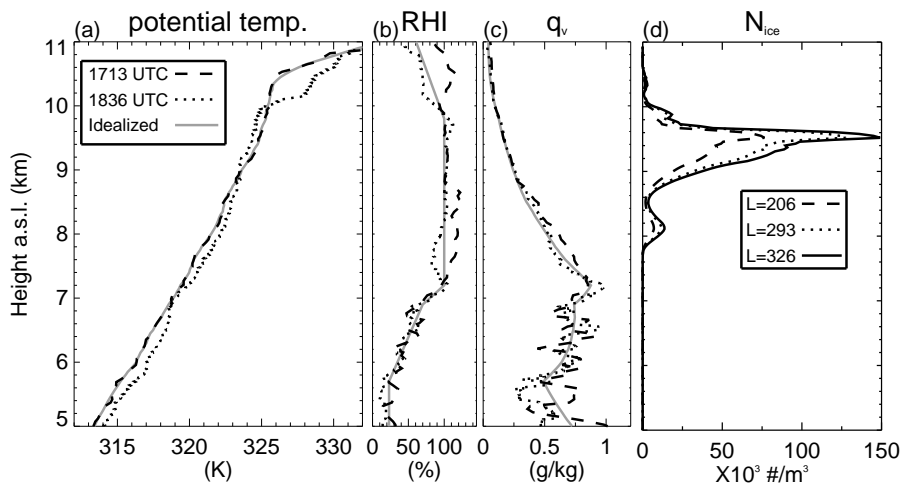


Fig. 10. (a, b, c) The atmospheric profiles measured at 17:13 (dashed) and 18:36 (dotted) UTC versus altitude a.s.l. The gray curves indicate the idealized profiles used as the initial conditions for the 1-D simulations. (d) The profiles of ice number concentration, N_{ice} , retrieved using the lidar backscatter profile measured at 17:32 UTC. In the calculation, the modified gamma distribution is used, μ is set to 7 and three values of L (326, 293, 206 cm^{-1}) are tested.

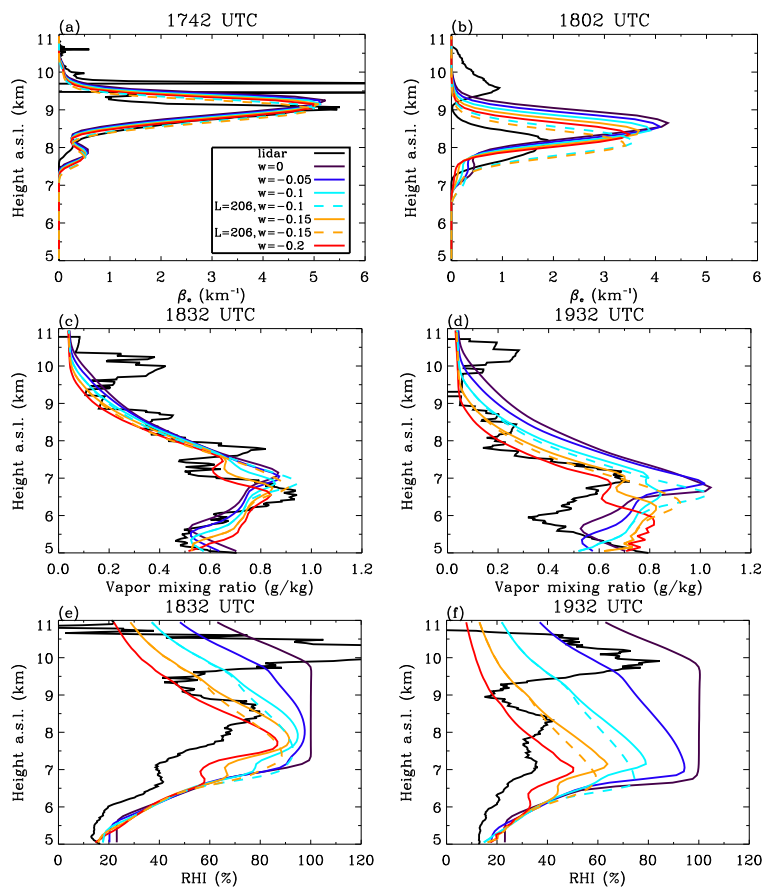


Fig. 11. Lidar measurements vs 1-D simulations at selected times. Panels (a, b) are the profiles of the volume extinction coefficient; (c, d) are the profiles of the vapour mixing ratio, and (e, f) are the profiles of RHI. In the simulations, L is 326 cm^{-1} except where otherwise noted.

Table 2. Results of test cases obtained with the 1-D model. The simulation using $w=0\text{m/s}$ is not listed because it compares poorly with the observation.

w (m/s)	L (cm^{-1})	$t=90$ min			$t=120$ min		
		(1) $\frac{\text{IWP}_0 - \text{IWP}}{\text{IWP}_0}$ %	(2) $\frac{\text{EIP}_7}{\text{EIP}_t}$ %	(3) $\frac{\text{EIP}_7}{\text{VP}_7}$ %	(1) $\frac{\text{IWP}_0 - \text{IWP}}{\text{IWP}_0}$ %	(2) $\frac{\text{EIP}_7}{\text{EIP}_t}$ %	(3) $\frac{\text{EIP}_7}{\text{VP}_7}$ %
−0.05	326	77	50	10	98	62	21
−0.10	326	98	45	11	100	59	20
−0.15	326	100	49	13	100	67	24
−0.20	326	100	59	16	100	76	27
−0.10	206	100	67	21	100	63	27
−0.15	206	100	68	22	100	64	27

moistening? In order to answer these questions several case studies were examined, which are summarised in Table 2. The definition of the parameters indicated in Table 2 is as follows:

- IWP is Ice Water Path;
- IWP_0 is Ice Water Path at $t=0$ (the initial time of the integration);
- EIP_7 is the Evaporated Ice Path between 6.5 and 7.5 km;
- EIP_t is the Evaporated Ice Path in the entire air column
- VP_7 is the Vapour Path between 6.5 and 7.5 km measured by *BASIL*.

The column labelled (1) in Table 2 ($\frac{\text{IWP}_0 - \text{IWP}}{\text{IWP}_0}$) is the fraction (expressed in percentage) of the initial ice water path that has been converted to water vapour in a given period of time. Thus, the product of column (1) and column (2) is the fraction (expressed in percentage) of the initial ice water path that is redistributed into the layer extending from 6.5 to 7.5 km at a given time. Column (3) (that is EIP_7/VP_7) tells how significant the “evaporated ice path” between 6.5 and 7.5 km is when compared to the measured vapour path in the same vertical interval.

The total water path (the sum of vapour path and ice path) is generally not a conservative quantity. For this case of rather limited vertical mass displacement, a very small error is introduced by taking the total water path as a conservative quantity. The results presented in Table 2 show that it is safe to conclude that the cloud moistens the layer between 6.5 and 7.5 km, regardless of the assumed magnitude of the vertical velocity. However, simulations driven by a stronger downdraft provide a better time evolution of the cloud in the sense that the simulated extinction coefficient is closer to the measured one.

Results are somewhat sensitive to the assumption of the duration of the downdraft. If the downdraft lasts, for ex-

ample, for 90 min, the redistribution plays a less significant role on the local vapour mass between 6.5 and 7.5 km, which translates into a smaller value of the ratio $\text{EIP}_7/\text{EIP}_t$. If the downdraft persists until $t=120$ min, the redistribution plays a more important role. From column (3) (EIP_7/VP_7), the cloud does contribute 10–22% at $t=90$ min and 20–27% at $t=120$ min of vapour mass. This indicates that the sedimentation-moistening has contributed significantly to the moist anomaly, but other factors are working as well.

5 Summary and conclusions

The paper considers the application of a Raman lidar system providing simultaneous measurements of temperature, water vapour mixing ratio and cloud optical properties. Raman lidar measurements performed on 6 September 2004 in the presence of cirrus clouds during the Italian phase of the EAQUATE experiment are reported and discussed. The variability of relative humidity inside and beneath the two layer cirrus cloud has been determined. Under-saturation conditions with respect to water and both ice super-saturation and under-saturation conditions are found inside clouds. Relative humidity in ice clouds is observed to increase with decreasing temperatures. Lidar measurements also reveal the presence of a humid layer beneath the cirrus clouds.

The synergistic use of the data derived from the ground based Raman Lidar and of the spectral radiances measured by the NAST-I Airborne Spectrometer provides evidence that it is possible to reconstruct the temporal evolution of the atmospheric cooling/heating rates in presence of observed cirrus cloud vertical structure. A large temperature gradient ($\sim 10\text{K/day}$) is found to develop between cloud top and bottom, but this radiative forcing effect is not sufficient to completely explain the ice cloud dissipation, and cloud microphysics needs to be accounted for. We have relied on a 1-D cloud microphysical model to describe the evolution of volume extinction coefficient, relative humidity and water vapour mixing ratio profiles observed beneath the cirrus

cloud, for a variety of imposed air vertical velocities and PSD. The initial conditions represent the measured state over Potenza at 17:32 UTC and the initial PSD is inferred from synergistic lidar and NAST-I observations.

The results show that it is safe to conclude that the cloud moistens the layer beneath the lower cloud deck, regardless of the assumed magnitude of the vertical velocity. Simulations driven by a stronger downdraft provide a better time evolution of the cloud, leading to simulated extinction coefficient values closer to the measured ones. The 1-D simulations indicate that the sedimentation-moistening has contributed significantly to the moist anomaly, but other factors are at work as well. This result supports the hypothesis that the mid-tropospheric humidification, observed by *BASIL* is a real feature which is strongly influenced by the sublimation of precipitating ice crystals.

Results illustrated in this study demonstrate that Raman lidars, like the one used in this study, can resolve the spatial and temporal scales required for the study of cirrus cloud microphysical processes and appears sensitive enough to reveal and quantify upper tropospheric humidification associated with cirrus cloud sublimation, ultimately offering the opportunity to improve the parameterization of cirrus clouds in dynamical models.

Acknowledgements. The NAST-I instrument is operated by NASA Langley Research Center (LaRC) with support from the University of Wisconsin-Madison. The SEVIRI images were obtained from the Eumetsat U-MARF archive at <http://archive.eumetsat.org/umarf/>. We wish to thank IMAA-CNR for the provision of radiosonde data.

Edited by: M. Petters

References

- Ansmann, A., Wandinger, U., Riebesell, M., Wietkamp, C., and Michaelis, W.: Independent measurements of extinction and backscatter profiles in cirrus clouds by using a combined Raman elastic-backscatter LIDAR, *Appl. Optics*, 31, 7113–7113, doi:10.1364/AO.31.007113, 1992.
- Behrendt, A. and Reichardt J.: Atmospheric temperature profiling in the presence of clouds with a pure rotational Raman lidar by use of an interference-filter-based polychromator, *Appl. Optics*, 39, 1372–1378, doi:10.1364/AO.39.001372, 2000.
- Behrendt, A.: Temperature measurements with lidar, in: *Lidar: Range-Resolved Optical Remote Sensing of the Atmosphere*, edited by: Weitkamp, C., 102, Springer Series in Optical Sciences, Springer, 273–305, 2005.
- Bhawar, R., Bianchini, G., Bozzo, A., Calvello, M. R., Cacciani, M., Carlotti, M., Castagnoli, F., Cuomo, V., Di Girolamo, P., Di Iorio, T., Di Liberto, L., di Sarra, A., Esposito, F., Fiocco, G., Fuà, D., Grieco, G., Maestri, T., Masiello, G., Muscari, G., Palchetti, L., Papandrea, E., Pavese, G., Restieri, R., Rizzi, R., Romano, F., Serio, C., Summa, D., Todini, G., and Tosi, E.: Spectrally resolved observations of Earth's emission spectrum in the H₂O rotation band, *Geophys. Res. Lett.*, 35, L04812, doi:10.1029/2007GL032207, 2008.
- Borbas, E., Moy, L., Seemann, S., Knuteson, R.O., Trigo, I., Antonelli, P., Li, J., Huang, H.L.: A global infrared land surface emissivity database and its validation. Symposium on Integrated Observing and Assimilation Systems for Atmosphere, Oceans, and Land Surface, 11th, San Antonio, TX, 14–18 January 2007, American Meteorological Society, Boston, Paper P2.7, 5285, 2007.
- Bozzo, A., Maestri, T., Rizzi, R., and Tosi, E.: Parameterization of single scattering properties of mid-latitude cirrus clouds for fast radiative transfer models using particle mixtures, *Geophys. Res. Lett.*, 35, L16809, doi:10.1029/2008GL034695, 2008.
- Chen, J.-P., McFarquhar, G. M., Heymsfield, A. J., and Ramanathan, V.: A modeling and observational study of the detailed microphysical structure of tropical cirrus anvils, *J. Geophys. Res.-Atmos.*, 102, 6637–6653, 1997.
- Chen, W.-N., Chiang, C.-W., and Nee, J.-B.: Lidar ratio and depolarization ratio for cirrus clouds, *Appl. Optics*, 41, 6470–6476, doi:10.1364/AO.41.006470, 2002.
- Clough, S. A. and Iacono, M. J.: Line-by-line calculations of atmospheric fluxes and cooling rates II: application to carbon dioxide, ozone, methane, nitrous oxide, and the halocarbons, *J. Geophys. Res.-Atmos.*, 100, 16519–16535, 1995.
- Comstock, J., Lin, R.-F., Starr, D. O., and Yang, P.: Understanding ice supersaturation, particle growth, and number concentration in cirrus clouds, *J. Geophys. Res.-Atmos.*, 113, D23211, doi:10.1029/2008JD010332, 2008.
- Cousins, D. and Gazarick, M. J.: NAST Interferometer Design and Characterization, Final Report, MIT Lincoln Laboratory Project Report NOAA-26, 13 July 1999.
- Di Girolamo, P., Marchese, R., Whiteman, D. N., and Demoz, B.: Rotational Raman Lidar measurements of atmospheric temperature in the UV, *Geophys. Res. Lett.*, 31, L01106, doi:10.1029/2003GL018342, 2004.
- Di Girolamo, P., Behrendt, A., and Wulfmeyer, V.: Pure rotational Raman lidar measurements of atmospheric temperature and extinction from space: performance simulations, *Appl. Optics*, 45, 2474–2494, doi:10.1364/AO.45.002474, 2006.
- Di Girolamo, P., Summa, D., and Ferretti, R.: Rotational Raman Lidar measurements for the characterization of stratosphere-troposphere exchange mechanisms, *J. Atmos. Ocean. Tech.*, 26(9), 1742–1762, doi:10.1175/2009JTECHA1253.1, 2009.
- Evans, K. F. and Stephens G. L.: A new polarized atmospheric radiative transfer model, *J. Quant. Spectrosc. Ra.*, 46, 412–423, doi:10.1016/0022-4073(91)90043-P, 1991.
- Ferrare, R. A., Browell, E. V., Ismail, S., Kooi, S. A., Brasseur, L. H., Brackett, V. G., Clayton, M. B., Barrick, J. D., Diskin, G. S., Goldsmith, J. E., Lesht, B. M., Podolske, J. R., Sachse, G. W., Schmidlin, F. J., Turner, D. D., Whiteman, D. N., Tobin, D. C., Miloshevich, L. M., Revercomb, H. L., Demoz, B. B., and Di Girolamo, P.: Characterization of Upper-Troposphere Water Vapor Measurements during AFWEX Using LASE, *J. Atmos. Ocean. Tech.*, 21(12), 1790–1808, doi:10.1175/JTECH-1652.1, 2004.
- Giannakaki, E., Balis, D. S., Amiridis, V., and Kazadzis, S.: Optical and geometrical characteristics of cirrus clouds over a Southern European lidar station, *Atmos. Chem. Phys.*, 7, 5519–5530, 2007,

- <http://www.atmos-chem-phys.net/7/5519/2007/>.
- Gierens, K., Schumann, U., Helten, M., Smit, H., and Marenco, A.: A distribution law for relative humidity in the upper troposphere and lower stratosphere derived from three years of MOZAIC measurements, *Ann. Geophys.*, 17, 1218–1226, 1999, <http://www.ann-geophys.net/17/1218/1999/>.
- Griaznov, V., Veselovskii, I., Di Girolamo, P., Korenskii, M., and Summa, D.: Spatial distribution of doubly scattered polarized laser radiation in the focal plane of a lidar receiver, *Appl. Optics*, 46, 6821–6830, doi:10.1364/AO.46.006821, 2007.
- Held, I. M. and Soden, B. J.: Water vapor feedback and global warming, *Annu. Rev. Energ. Env.*, 25, 441–475, doi:10.1146/annurev.energy.25.1.441, 2000.
- Lin, R.-F., Starr, D. O., Reichardt, J., and DeMott, P. J.: Nucleation in synoptically forced cirrostratus, *J. Geophys. Res.-Atmos.*, 110, D08208, doi:10.1029/2004JD005362, 2005.
- Liou, K. N.: Influence of cirrus clouds on weather and climate processes: a global perspective, *Mon. Weather Rev.*, 114, 1167–1199, 1986.
- Luo, Y., Krueger, S. K., Mace, G., and Xu, K.-M.: Cirrus cloud properties from a cloud-resolving model simulation compared to cloud radar observations, *J. Atmos. Sci.*, 60, 510–525, 2003.
- Kolorev, A. and Isaac, G.: Relative humidity in liquid, mixed-phase, and ice clouds, *J. Atmos. Sci.*, 63, 2865–2880, doi:10.1175/JAS3784.1, 2006.
- Maestri, T., Rizzi, R., and Smith, J. A.: Spectral infrared analysis of a cirrus cloud based on Airborne Research Interferometer Evaluation System (ARIES) measurements, *J. Geophys. Res.*, 110(D6), D06111, doi:10.1029/2004JD005098, 2005.
- Maestri, T., Di Girolamo, P., Summa, D., and Rizzi, R.: Synergistic use of a ground based RAMAN Lidar and the NAST-I Airborne Spectrometer in clear and cloudy sky conditions 'EAQUATE, ITALY 2004, *Atmos. Res.*, in review, 2009.
- Maestri, T. and Holz, R. E.: Retrieval of cloud optical properties from multiple infrared hyperspectral measurements: a methodology based on a line-by-line multiple scattering code, *IEEE T. Geosci. Remote*, 47(9), 2413–2426, doi:10.1109/TGRS.2009.2016105, 2009.
- Mitchell, D. L. and Arnott, W. P.: A model predicting the evolution of ice particle size spectra and radiative properties of cirrus clouds. Part II: dependence of absorption and extinction on ice crystal morphology, *J. Atmos. Sci.*, 51, 817–832, 1994.
- Mona, L., Cornacchia, C., D'Amico, G., Di Girolamo, P., Pappalardo, G., Pisani, G., Summa, D., Wang, X., and Cuomo, V.: Characterization of the heterogeneity of the humidity and cloud fields as observed from a cluster of ground-based lidar systems, *Q. J. Roy. Meteor. Soc.*, 133, 257–271, doi:10.1002/qj.160, 2007.
- Ovarlez, J., Gayet, J.-F., Gierens, K., Ström, J., Ovarlez, H., Auriol, F., Busen, R., and Schumann, U.: Water vapor measurements inside cirrus clouds in Northern and Southern Hemispheres during INCA, *Geophys. Res. Lett.*, 29(16), 1813, doi:10.1029/2001GL014440, 2002.
- Platt, C. M. R., Gimmestad, G. G., Young, S. A., Carswell, A. I., Pal, S. R., McCormick, M. P., Whinker, D. M., Del Gusta, M., Stefanutti, L., Eberhard, W. L., Hardesty, M., Flamant, P. H., Valentin, R., Forgan, B., Jager, H., Khmelevstov, S. S., Kolev, I., Kaprieolev, B., Da-ren Lu, Sassen, K., Shamanaev, V. S., Uchino, O., Mizuno, Y., Wandinger, U., Weitkamp, C., Ansmann, A., and Wooldridge, C.: The experimental cloud lidar pilot study (ECLIPS) for cloud-radiation research, *B. Am. Meteorol. Soc.*, 75, 1635–1654, 1994.
- Ramanathan, V., Pitcher, E. J., Malone, R. C., and Blackmon, M. L.: The response of a spectral general circulation model to refinements in radiative processes, *J. Atmos. Sci.*, 40, 605–630, 1983.
- Ramaswamy, V. and Detwiler, A.: Interdependence of radiation and microphysics in cirrus clouds, *J. Atmos. Sci.*, 43, 2289–2301, 1986.
- Rizzi, R., di Pietro, P., Loffredo, G., and Smith, J. A.: Comparison of measured and modeled stratus cloud infrared spectral signatures, *J. Geophys. Res.*, 106(D24), 34109–34119, doi:10.1029/2001JD000437, 2001.
- Sinha, A. and Harries, J. E.: Water vapour and greenhouse trapping: the role of far infrared absorption, *Geophys. Res. Lett.*, 22, 2147–2150, 1995.
- Starr, D. O'C. and Wylie, D. P.: The 27–28 October 1986 FIRE cirrus case study: meteorology and clouds, *Mon. Weather Rev.*, 118, 2259–2287, 1990.
- Stephens, G. L., Tsay, S.-C., Stackhouse, P. W., and Flatau, P. J.: The relevance of the microphysical and radiative properties of cirrus clouds to climate and climatic feedback, *J. Atmos. Sci.*, 47, 1742–1754, 1990.
- Ström, J., Seifert, M., Kärcher, B., Ovarlez, J., Minikin, A., Gayet, J.-F., Krejci, R., Petzold, A., Auriol, F., Haag, W., Busen, R., Schumann, U., and Hansson, H. C.: Cirrus cloud occurrence as function of ambient relative humidity: a comparison of observations obtained during the INCA experiment, *Atmos. Chem. Phys.*, 3, 1807–1816, 2003, <http://www.atmos-chem-phys.net/3/1807/2003/>.
- Taylor, J. P., Smith, W. L., Cuomo, V., Larar, A. M., Zhou, D. K., Serio, C., Maestri, T., Rizzi, R., Newman, S., Antonelli, P., Mango, S., Di Girolamo, P., Esposito, F., Grieco, G., Summa, D., Restieri, R., Masiello, G., Romano, F., Pappalardo, G., Pavese, G., Mona, L., Amodeo, A., and Pisani, G.: EAQUATE An International Experiment For Hyper-spectral Atmospheric Sounding Validation, *B. Am. Meteorol. Soc.*, 89(2), 203–218, doi:10.1175/BAMS-89-2-203, 2008.
- Whiteman, D. N., Demoz, B., Di Girolamo, P., Comer, J., Veselovskii, I., Evans, K., Wang, Z., Cadirola, M., Rush, K., Schwemmer, G., Gentry, B., Melfi, S. H., Mielke, B., Venable, D., and Van Hove, T.: Raman Lidar Measurements During the International H₂O Project. I. Instrumentation and Analysis Techniques, *J. Atmos. Ocean. Tech.*, 23, 157–169, 2006a.
- Whiteman, D. N., Demoz, B., Di Girolamo, P., Comer, J., Veselovskii, I., Evans, K., Wang, Z., Sabatino, D., Schwemmer, G., Gentry, B., Lin, R., Behrendt, A., Wulfmeyer, V., Browell, E., Ferrare, R., Ismail, S., and Wang, J.: Raman Lidar Measurements During the International H₂O Project. II. Case Studies, *J. Atmos. Ocean. Tech.*, 23, 170–183, 2006b.